



**HAL**  
open science

# Overpressure generation by smectite dehydration in sedimentary basins constrained by salinity dilution and stable isotopes

Joachim Tremosa, Eric Gaucher, H el ene Gailhanou

► **To cite this version:**

Joachim Tremosa, Eric Gaucher, H el ene Gailhanou. Overpressure generation by smectite dehydration in sedimentary basins constrained by salinity dilution and stable isotopes. *Applied Geochemistry*, 2021, 131, pp.105035. 10.1016/j.apgeochem.2021.105035 . hal-03745479

**HAL Id: hal-03745479**

**<https://brgm.hal.science/hal-03745479>**

Submitted on 2 Aug 2023

**HAL** is a multi-disciplinary open access archive for the deposit and dissemination of scientific research documents, whether they are published or not. The documents may come from teaching and research institutions in France or abroad, or from public or private research centers.

L'archive ouverte pluridisciplinaire **HAL**, est destin ee au d ep ot et  a la diffusion de documents scientifiques de niveau recherche, publi es ou non,  emanant des  tablissements d'enseignement et de recherche fran ais ou  trangers, des laboratoires publics ou priv es.



Distributed under a Creative Commons Attribution - NonCommercial 4.0 International License

1 Overpressure generation by smectite dehydration in  
2 sedimentary basins constrained by salinity dilution  
3 and stable isotopes

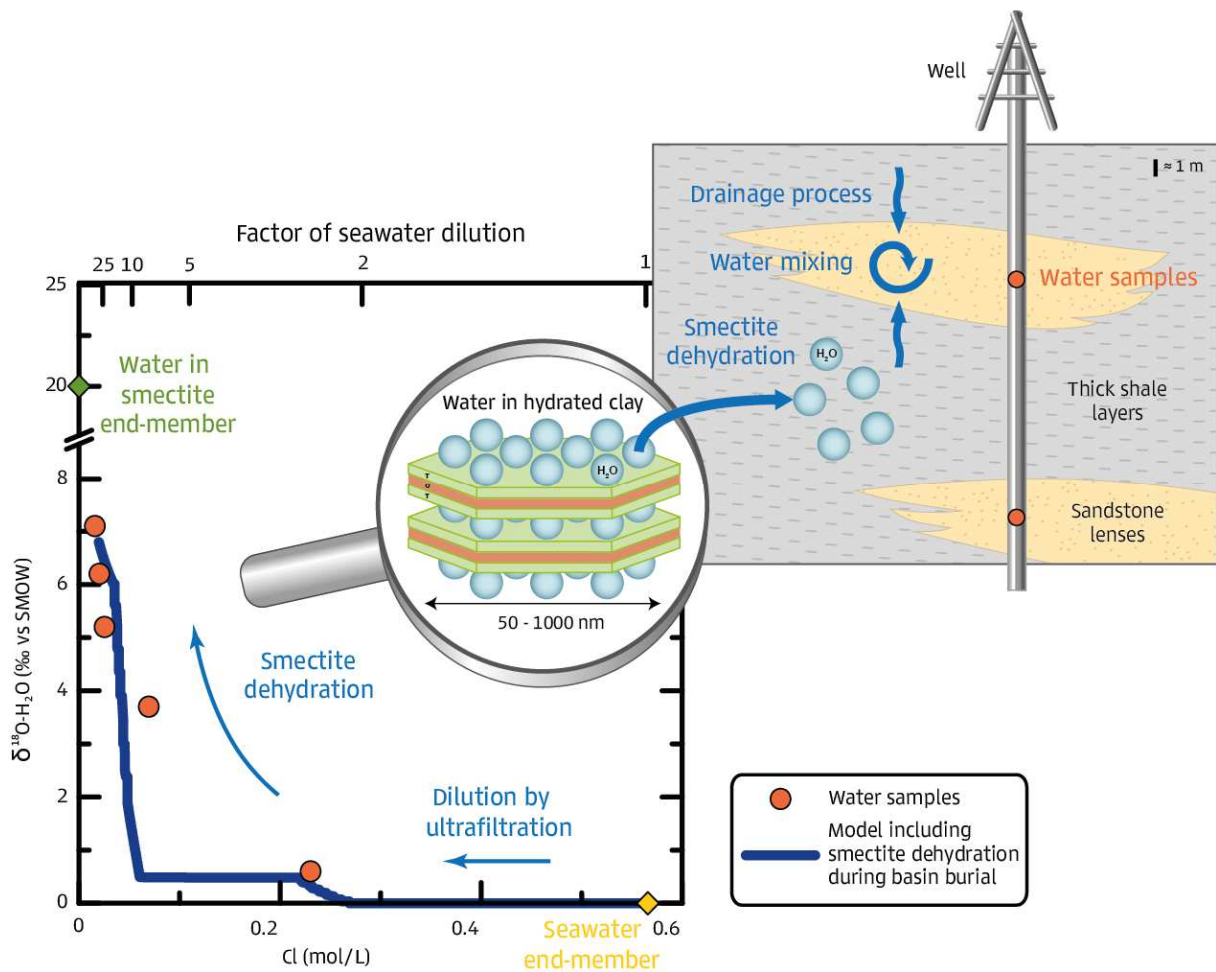
4  
5 *Joachim Tremosa<sup>1\*</sup>, Eric C. Gaucher<sup>2</sup>, H el ene Gailhanou<sup>1</sup>*

6  
7 *1. BRGM, 3 avenue Claude Guillemin, BP 36009, 45060 Orl ans, France*

8 *2. TOTAL S.A., CSTJF, Avenue Larribau, 64018 Pau, France*

9 *\*corresponding author: j.tremosa@brgm.fr; (phone n : +33238643204)*

10 Graphical abstract



11

## 12 Abstract

13 The water released by smectite dehydration because of pressure and temperature increase during  
14 burial of claystone or clay-rich mudstone in sedimentary basins can generate overpressure and  
15 change the water salinity. Up until now, a clear distinction has been lacking between the water  
16 fraction produced by compaction and the water fraction produced by thermodynamic dehydration.  
17 Smectite dehydration is mentioned in the literature in pore pressure prediction or as a hypothesis for  
18 water freshening but direct evidence is missing.

19 Here, we bring this evidence by linking the  $\delta^{18}\text{O}\text{-H}_2\text{O}$  water isotopic signature, salinity evolution and  
20 overpressure generation to the spatial and temporal fluid budget in a sedimentary pile involving  
21 smectite dehydration. Water samples indicating an increase in  $\delta^{18}\text{O}\text{-H}_2\text{O}$  and a salinity decrease were  
22 sampled deep offshore in the Gulf of Guinea in sandstone lenses intercalated within shale layers. By  
23 using a numerical coupled approach, we were able to reproduce the fluid evolution by modelling  
24 smectite dehydration based on thermodynamic considerations during the burial of the sedimentary  
25 pile and the associated pressure and temperature evolution over geological ages.

26

## 27 Introduction

28 An understanding of fluid migration and trapping over the history of sedimentary basins is needed  
29 for the sustainable and cost-effective exploitation of geothermal and oil and gas subsurface  
30 resources as it ensures a more accurate evaluation of the resource and anticipation of its evolution.  
31 In deep geological settings considering the impact of clay-rich sediments on the fluid migration and  
32 pressure evolution remain a challenge. Migration of fluids and solutes is complexly impacted in deep  
33 claystones because of their low permeability, their membrane behaviour that can restrict the  
34 transport of waters and solutes and because of the water/rock interactions.

35 Smectite dehydration in sedimentary basins is sometimes cited as a process that can generate  
36 abnormal pressure conditions (Audet, 1995; Bruce, 1984; Tanikawa et al., 2008; Tremosa et al., 2020)  
37 or as a freshening mechanism. However, direct evidence of the influence of smectite dehydration on  
38 fluid evolution at the scale of the basin or formation was still missing. Smectite dehydration consists  
39 in the loss of interlayer water within smectite crystal that occurs with temperature and pressure  
40 increase (Figure 1). The term 'smectite dehydration' also refers to the loss of water during the  
41 smectite-to-illite transformation and attention was mainly paid to this latter process in sedimentary  
42 basins. In both cases, when smectite dehydration of interlayer water occurs or when the smectite  
43 structure evolves to an illite structure, the interlayer water is released to the shale porosity. The

44 smectite dehydration process must not be confused with the water produced by the compaction of  
45 the clayey formations. In the latter process, interstitial water is drained by applying burial stress to  
46 the formations.

47 Overpressures in sedimentary basins are hydrodynamic phenomena involving various coupled  
48 geological processes over the basin history (Neuzil, 1995). When the different hydraulic, mechanical,  
49 thermal and chemical couplings are considered, the interpretation of overpressure generation and  
50 dissipation to obtain the present-day pressure profile provides good insights into the fluid migration  
51 and budget in the basin. At the basin scale, the expression of smectite dehydration can be recorded  
52 by the pore pressure (Bruce, 1984; Tanikawa et al., 2008; Tremosa et al., 2020), but the  
53 interpretation of the origin of the pore pressure profile generally remains uncertain (Bjørlykke et al.,  
54 2010) with smectite dehydration acting as an additional cause of overpressure (Audet, 1995;  
55 Tremosa et al., 2020). Stable oxygen isotopic data are also commonly used to document the pore  
56 fluid history in sedimentary basins (Hanor, 1994), taking into account the contribution of the  
57 different sources of water. Pore fluid enriched in  $^{18}\text{O}$  concomitantly to a decrease in salinity is often  
58 interpreted as the consequence of smectite dehydration (Boschetti et al., 2016; Clayton et al., 1966;  
59 Franks & Uchtyl, 2016; Macpherson, 1992; Morton & Land, 1987; Nicot et al., 2018; Wilkinson et al.,  
60 1992). However, this interpretation of smectite dehydration influencing the  $\delta^{18}\text{O}\text{-H}_2\text{O}$  isotopic  
61 signature and salinity is generally not based on a volume budget of water released by smectite  
62 minerals and its mixing with porewater in the sedimentary pile. Moreover, the thermodynamics of  
63 smectite dehydration are rarely checked (Colten-Bradley, 1987; Vidal & Dubacq, 2009).  
64 Consequently, the effect of smectite dehydration remains a hypothesis that requires to be tested by  
65 a coupled approach, combining burial, smectite dehydration and water freshening considerations.

66 Smectite dehydration is also documented in mud volcanoes (Dählmann & Lange, 2003; Hensen et al.,  
67 2007) and in subduction zones (Kastner et al., 1993), where correlations are observed between water  
68 freshening and an increase in the  $\delta^{18}\text{O}\text{-H}_2\text{O}$  isotopic signature, and are explained by smectite  
69 dehydration. These studies generally relate water release to smectite-to-illite transformation, but a  
70 few of them focus on the dehydration of interlayer smectite (Fitts & Brown, 1999; Hüpers & Kopf,  
71 2012). In these studies, smectite dehydration was induced in laboratory experiments that considered  
72 pressure and temperature conditions of convergent margins. In subduction zones and mud  
73 volcanoes, smectite dehydration during illitisation has also been considered in the fluid budget of  
74 numerical analyses to explain the observed water freshening with depth (Bekins et al., 1995; Brown  
75 et al., 2001; Henry & Bourlange, 2004; Hüpers et al., 2019; Saffer & McKiernan, 2009; Vanneste et al.,  
76 2011). However, these studies only consider the temperature dependence of the smectite-to-illite  
77 transformation, overlooking smectite dehydration.

78 In our study, we tested the effect of smectite dehydration on the  $\delta^{18}\text{O}\text{-H}_2\text{O}$  isotopic signature, the  
79 evolution of pore fluid salinity and overpressure generation in a sedimentary pile in the Gulf of  
80 Guinea. The  $\delta^{18}\text{O}\text{-H}_2\text{O}$  signature and the salinity are two records of smectite dehydration and of the  
81 volume of water that is consequently released in the sediments. Smectite dehydration is described  
82 by considering a consistent thermodynamic model as a function of pressure and temperature  
83 evolution during the burial of the sedimentary pile. The water budget then accounts for the release  
84 of water by smectite dehydration depending on the geometry, pressure, temperature and properties  
85 of the sedimentary pile and the timing of this water release.

## 86 Methods

### 87 Sampling and analyses

88 Field data were obtained from a well, drilled to explore the petroleum potential of the Gulf of  
89 Guinea. This well is located about 50 km from the coast, at a sea depth of about 2000 m. The drilling  
90 penetrated through a sediment thickness of about 2700 m, from the seafloor. The main objective of  
91 the well was to identify the Upper Cretaceous post-rift series and, in particular, the sandstone  
92 reservoirs in turbidite systems. During the drilling operations and the following tests, a large set of  
93 data was obtained regarding geology, lithology, mineralogy, pressure and temperature conditions  
94 and fluid composition in the reservoirs, amongst other information. The following data from the well  
95 were used for hydrogeological interpretation and the modelling of the present study:

- 96 • The lithological and composite logs of the well at a scale of 1:500 were used to establish the  
97 lithological profile and the meshing.
- 98 • Biostratigraphic dating was available, based on foraminifera, nanoplankton and pollens  
99 identified on cuttings and cores. This dating was used together with the sediment thickness  
100 at the deposition to calculate the sedimentation rate.
- 101 • The formation pressure, corresponding to the fluid pressure, was measured in the well by 87  
102 measurements using Schlumberger Modular Formation Dynamics Tester of which 28 gave  
103 good quality results. The pressure was hydrostatic down to the Campanian deposit basis. A  
104 moderate fluid overpressure was measured below, corresponding to an apparent density of  
105 1250 to 1300  $\text{kg}\cdot\text{m}^{-3}$  in Turonian and Santonian levels ( $\rho = P/g \cdot z$ ). The Turonian reservoirs  
106 separated by shale layers are not hydraulically connected. In addition, the shale pressure was  
107 measured to be close to the reservoir pressure.
- 108 • A temperature gradient of about 4.4 °C/100 m was measured between the seabed (4 °C) and  
109 the well foot during electrical logs.

- 110 • The mineralogy and petrography of samples presenting different facies and ages were  
111 determined through petrographic studies on 43 samples, by quantitative mineralogy  
112 analyses (bulk rock XRD-XRF, CEC, density, organic carbon and sulphur analyses and XRD clay  
113 fraction analyses) on 66 samples and by complementary mineralogical analyses on clay  
114 mineral phases (electron microprobe) on 3 samples.
- 115 • Five water samples were taken during MDT tests in the sandstone reservoir at depths  
116 between 2000 and 2600 m below the seafloor, allowing the determination of the chemical  
117 and isotopic ( $\delta^{18}\text{O}$  and  $\delta^2\text{H-H}_2\text{O}$ ,  $^{87}\text{Sr}/^{86}\text{Sr}$ ,  $\delta^{34}\text{S}$  and  $\delta^{18}\text{O-SO}_4$  and  $\delta^7\text{Li}$ ) composition of these  
118 waters.

### 119 Thermodynamic model for smectite dehydration

120 The chemical composition of pure smectite was determined for a shale sample of the Turonian age  
121 from the well, by performing 150 electron microprobe analyses on the  $< 2 \mu\text{m}$  clay fraction. Among  
122 them, the smectite compositions, expressed on a structural basis of  $\text{O}_{10}(\text{OH})_2$ , were selected using  
123  $\text{M}^+-4\text{Si}-\text{R}^{2+}$  diagrams (Meunier & Velde, 1989) ( $\text{M}^+$  = layer charge of ideal micas,  $4\text{Si}$  = maximum Si  
124 content of the tetrahedral sheet,  $\text{R}^{2+}$  = amount of bivalent cations in the octahedral position),  
125 following which the compositions associated with mixtures of clay minerals and/or other silicate  
126 minerals could be discarded. The following mean composition for smectite was obtained  
127  $(\text{Na}_{0.085}\text{K}_{0.180}\text{Ca}_{0.037})(\text{Si}_{3.809}\text{Al}_{0.191})(\text{Al}_{1.720}\text{Mg}_{0.090}\text{Fe}^{2+}_{0.256})\text{O}_{10}(\text{OH})_2$ , with a molar mass of 379.51 g/mol. For  
128 sake of simplicity in the application of the thermodynamic model in the burial model, the Na  
129 homoionized form of the smectite was considered.

130 The thermodynamic smectite dehydration model (Vidal & Dubacq, 2009) adapted for use in  
131 PHREEQC geochemical calculation code (Tremosa et al., 2020) considers binary solid solutions  
132 between hydrated smectite end-members with 1, 2 or 3 layers of water, which respectively contain  
133 2, 4 and 7 moles of interlayer water per mole of smectite (on a structural basis  $\text{O}_{10}(\text{OH})_2$ ), and  
134 anhydrous smectite. The description of smectite dehydration then involves the three following binary  
135 solid solutions, where A refers to anhydrous, and 1w, 2w and 3w refer to 1, 2 and 3 layers of water,  
136 respectively:

- 137 - Smect\_Na.A – Smect\_Na.1w  
138 - Smect\_Na.A – Smect\_Na.2w  
139 - Smect\_Na.A – Smect\_Na.3w

140

141 The deployment of this smectite dehydration model required calculating the thermodynamic  
 142 properties ( $G$ ,  $H$ ,  $S$ ,  $C_p$ ,  $V$ ) of the anhydrous end-member (Blanc et al., 2015) and of the hydrated  
 143 smectite end-members (Vidal & Dubacq, 2009) (Table 1) as well as the dependence of the smectite  
 144 equilibrium constant on temperature (Table 2). The interaction parameters of the non-ideal solid  
 145 solution estimated for montmorillonites were used (Vidal & Dubacq, 2009). So, Margules parameters  
 146 of -10 kJ are considered for solid solutions between anhydrous smectite and the three hydrated  
 147 smectite end-members.

148 Preferential stability domains of the different hydrated smectite end-members were calculated  
 149 depending on the pressure and temperature conditions. The transition pressure and temperature  
 150 from a hydrated smectite end-member to a less hydrated smectite were then determined and used  
 151 in the model coupling burial and dehydration. For a given smectite, three stability domains were then  
 152 defined corresponding to the pressure and temperature conditions where the solid solution with 3  
 153 layers of water, 2 layers of water and 1 layer of water are in play. The stability domains for Na  
 154 smectite from the sedimentary pile are delimited by the following functions:

155 - Transition Smect\_Na.3w  $\rightarrow$  Smect\_Na.2w according ( $P_{tr1}, T_{tr1}$ ) :

156  $P_{tr1} = 102.53 T_{tr1} - 2843.9 \quad (r^2 = 0.990)$

157

158 - Transition Smect\_Na.2w  $\rightarrow$  Smect\_Na.1w according ( $P_{tr2}, T_{tr2}$ ) :

159  $P_{tr2} = 201.25 T_{tr2} - 20942 \quad (r^2 = 0.968)$

160 , with  $P_{tr}$  expressed in bar and  $T_{tr}$  in °C.

161 *Table 1 : Thermodynamic properties estimated for the smectite identified in the well and expressed as Na homoionized*  
 162 *smectite at 1.013 bar and 298.15 K. Clay mineral  $C_p(T)$  functions are expressed as  $C_p(T) = A + B \cdot 10^{-3} T + C \cdot 10^5 T^{-2}$ , where A, B*  
 163 *and C are Maier-Kelley coefficients.*

	$m_n H_2O$	$\Delta G_f^\circ$	$\Delta H_f^\circ$	$\delta H_f^\circ m_n H_2O$	$S^\circ$	$V^\circ$	$C_p(25^\circ C)$	A	B	C
	(mol/O <sub>10</sub> )	kJ/mol	kJ/mol	kJ/mol	J/mol/K	cm <sup>3</sup> /mol	J/mol/K	J/mol/K	J/mol/K <sup>2</sup>	J/mol*°K
Smect_Na.A	0	-5277.00	-5641.05		293.60	134.32	314.25	329.41	235.20	-75.82
Smect_Na.1w	2	-5762.50	-6232.85	293.85	403.60	168.56	402.23	418.09	284.52	-89.50
Smect_Na.2w	4	-6239.71	-6816.35	291.75	513.60	202.81	490.21	506.76	333.84	-103.19
Smect_Na.3w	7	-6951.26	-7687.34	290.33	678.60	250.75	622.19	639.77	407.82	-123.72

164

165 *Table 2 : Temperature dependence of the equilibrium constant ( $\log_{10} K$ ) for the dissolution of the identified Na smectite in*  
 166 *water, at 298.15 K and 1.013 bar.  $\log_{10} K = A_1 + A_2 * T + A_3 / T + A_4 * \log(T) + A_5 / T^2$*

	$m_n H_2O$	$\log_{10} K$	A1	A2	A3	A4	A5	Dissolution reaction
Smect_Na.A	0	4.78	-1.2871864E+03	-2.2190924E-01	6.9174286E+04	4.6807708E+02	-2.8539614E+06	$Na_{0.339}(Si_{3.809}Al_{0.191})(Al_{1.72}Mg_{0.09}Fe_{0.256})O_{10}(OH)_2 + 6.764H^+ + 3.236H_2O = 1.911Al^{+++} + 0.256Fe^{++} + 0.09Mg^{++} + 0.339Na^+ + 3.809H_4SiO_4$

Smect_Na.1w	2	2.82	-1.2400371E+03	-2.1299471E-01	6.5227041E+04	4.5146250E+02	-2.6249665E+06	Na <sub>0.339</sub> (Si <sub>3.809</sub> Al <sub>0.191</sub> )(Al <sub>1.72</sub> Mg <sub>0.09</sub> Fe <sub>0.256</sub> )O <sub>10</sub> (OH) <sub>2</sub> :2H <sub>2</sub> O + 6.764H <sup>+</sup> + 1.236H <sub>2</sub> O = 1.911Al <sup>+++</sup> + 0.256Fe <sup>++</sup> + 0.09Mg <sup>++</sup> + 0.339Na <sup>+</sup> + 3.809H <sub>4</sub> SiO <sub>4</sub>
Smect_Na.2w	4	2.30	-1.1928878E+03	-2.0408019E-01	6.1713440E+04	4.3484792E+02	-2.3959717E+06	Na <sub>0.339</sub> (Si <sub>3.809</sub> Al <sub>0.191</sub> )(Al <sub>1.72</sub> Mg <sub>0.09</sub> Fe <sub>0.256</sub> )O <sub>10</sub> (OH) <sub>2</sub> :4H <sub>2</sub> O + 6.764H <sup>+</sup> = 1.911Al <sup>+++</sup> + 0.256Fe <sup>++</sup> + 0.09Mg <sup>++</sup> + 0.339Na <sup>+</sup> + 3.809H <sub>4</sub> SiO <sub>4</sub> + 0.764H <sub>2</sub> O
Smect_Na.3w	7	2.28	-1.1246081E+03	-1.9110531E-01	5.6792159E+04	4.1082120E+02	-2.0593250E+06	Na <sub>0.339</sub> (Si <sub>3.809</sub> Al <sub>0.191</sub> )(Al <sub>1.72</sub> Mg <sub>0.09</sub> Fe <sub>0.256</sub> )O <sub>10</sub> (OH) <sub>2</sub> :7H <sub>2</sub> O + 6.764H <sup>+</sup> = 1.911Al <sup>+++</sup> + 0.256Fe <sup>++</sup> + 0.09Mg <sup>++</sup> + 0.339Na <sup>+</sup> + 3.809H <sub>4</sub> SiO <sub>4</sub> + 3.764H <sub>2</sub> O

167

168 Model coupling burial, dehydration and water freshening

169 The SURP code (Tremosa et al., 2020), a thermo-hydro-mechanical model coupled with chemical  
170 reactivity, was used to calculate the pore pressure evolution during the burial of a sedimentary pile  
171 under the combined effects of mechanical compaction, thermal expansion, water production by  
172 mineralogical reactions and water flow. This model relies on the resolution of the continuity equation  
173 in a porous medium where the variation of fluid mass depends on the changes in fluid pressure,  
174 mechanical stress and temperature over time. A source term is added to the water balance to  
175 consider the coupling with production and consumption of water by mineralogical reactions. The  
176 coupled flow equation can be expressed as follows:

$$177 \quad Ss' \frac{\partial P}{\partial t} - Ss' \xi \frac{d\sigma_{zz}}{dt} - \rho_f g \Lambda' \frac{\partial T}{\partial t} = \nabla \left[ g \frac{k \rho_f}{\mu_f} (\nabla P - \rho_f g \nabla z) \right] + \Gamma$$

178 where,  $S_s'$  is the unidimensional specific storage coefficient ( $m^{-1}$ ),  $P$  is the pore pressure (Pa),  $t$  is the  
179 time (s),  $\xi$  is the unidimensional loading coefficient (dimensionless),  $\sigma_{zz}$  is the total vertical stress (Pa),  
180  $\rho_f$  is the fluid density ( $kg \cdot m^{-3}$ ),  $g$  is the acceleration constant due to gravity ( $9.81 \text{ m} \cdot s^{-2}$ ),  $\Lambda'$  is the  
181 thermal response coefficient ( $^{\circ}C^{-1}$ ),  $T$  is the temperature ( $^{\circ}C$ ),  $\nabla z$  is (0,0,1) if the  $z$  axis is orientated  
182 downward,  $\mu_f$  is the fluid dynamic viscosity (Pa.s) and  $\Gamma$  is a source term corresponding to input or  
183 withdrawal of water in the porosity.

184 The chemical and isotopic evolutions of the water in the sandstone reservoirs were calculated by  
185 reproducing the mixing of sandstone water with water coming from the surrounding shale layers. For  
186 that, the water produced by smectite dehydration in the cells of the underlying and overlying shale  
187 layers was summed and mixed as fresh water in the water filling the sandstone layer. This mixing was  
188 performed during the PHREEQC operations of the SURP Python-PHREEQC coupling, using the  
189 keyword 'MIX' and considering the following mixing factor  $F_{mix}^{dehydration}$ :

$$190 \quad F_{mix}^{dehydration} = \frac{\sum \text{mass of dehydration water}}{\text{sandstone thickness} \times \rho_f \times n}$$



191 where,  $n$  is the porosity.

192 This mixing factor allows the evolution of the isotopic signature to be calculated by mixing the  
193 sandstone reservoir water which initially has a  $\delta^{18}\text{O-H}_2\text{O}$  signature of 0 ‰, corresponding to connate  
194 seawater, with water released by smectite dehydration with a  $\delta^{18}\text{O-H}_2\text{O}$  signature of +20 ‰ (Savin &  
195 Lee, 1988; Sheppard & Gilg, 1996). No isotopic fractionation was considered during dehydration  
196 reactions.

197 The dilution of sandstone reservoir water due to a flow of fresh water, i.e. by ultrafiltration in the  
198 shale or leakage, modifies the water salinity when the system becomes hydraulically closed. In this  
199 way, a dilution factor was applied to the water filling the sandstone reservoirs when the intrinsic  
200 permeability of the overlying shale layer was lower than  $10^{-20}$  m<sup>2</sup>. As long as the system was  
201 hydraulically open, it was assumed that the inflow of fresh water was equilibrated by advective  
202 mixing and a decrease in salinity cannot be observed. The dilution factor applied in the sandstone  
203 layer was adjusted to fit the observed salinity decrease.

204 The model mesh was built from the well log, and mineralogy and parameter profiles. The 2700 m  
205 thick sedimentary pile was divided into 82 successive lithological layers. The thickness of these  
206 lithological layers can vary between 2 m, for sandstone layers intercalated between shales, and 683  
207 m, for shallow sediments not concerned by the mechanisms under study. A backstripping or  
208 decompaction model (Sclater & Christie, 1980) was applied to calculate the thickness of each  
209 lithological layer at the time of its deposit. The calculated thickness of the uncompacted sedimentary  
210 pile is about 4400 m. Each lithological layer was then sliced into several meshes if the thickness of the  
211 uncompacted layer was greater than 10 m. The geometry of the sedimentary pile is therefore  
212 described by 411 meshes of initial thickness varying between 2.2 and 19.4 m. Sedimentation rates  
213 (Table 3) were calculated from the uncompacted thickness of sediments and the biostratigraphic  
214 dating for the well. The most significant sedimentation event occurred during the Santonian age,  
215 with a sedimentation rate of 340 m/My.

216

217 *Table 3: Sedimentation rates for forward modelling of IVOIRE-1X sediment deposition.*

Geological age		Sedimentation rate (m/My)
Since Miocene	15.97 My to present	60
Middle Eocene and Oligocene	41.2 My to 15.97 My	0
Paleocene and Middle Eocene	66 My to 41.2 My	20.4
Campanian and Maastrichtian	83.6 My to 66 My	52.5
Santonian	86.3 My to 83.6 My	340.1
Coniacian	89.8 My to 86.3 My	34.8
Turonian	93.9 My to 89.8 My	47.7
Cenomanian	100.5 to 93.9 My	39.4
Albian	113 to 100.5 My	40

218

219 Hydraulic and mechanical calculation parameters and initial content in smectite are reported in Table  
 220 4. In terms of hydraulic boundary conditions, hydrostatic conditions are considered in the layers of  
 221 the sedimentary pile above the roof of the measured overpressure. A no-flow Neumann boundary  
 222 condition is taken on the basis of the modelled sedimentary pile. This model considers a constant  
 223 temperature gradient with depth (0.0446 °C/m) based on the present-day geothermal gradient,  
 224 which is a simplification.

225

226 Table 4: Calculation parameters used in SURP modelling. 'sh', 'shsd' and 'sd' respectively correspond to the 'shale', 'shaly-  
 227 sandstone' and 'sandstone' facies encountered in the IVOIRE-1X sedimentary pile.  $n$  is porosity and  $e$  is the void ratio.

<b>Intrinsic permeability <math>k</math> (<math>m^2</math>)</b>	$\text{'sh'} : k = \frac{\left(\frac{n}{(1-n) 40 \times 2720}\right)^2}{3 n^{-3}}$ $\text{'shsd'} : k = \frac{\left(\frac{n}{(1-n) 40 \times 2680}\right)^2}{3 n^{-3}}$ $\text{'sd'} : k = 9.87 \cdot 10^{-13} \times 0.03 n^3$
<b>Biot coefficient <math>\alpha</math> (dimensionless)</b>	$\alpha = 1 - (1 - n)^{3.8}$
<b>Poisson ratio <math>\nu</math> (dimensionless)</b>	$\nu = 0.3$
<b>Young modulus <math>E</math> (GPa)</b>	$E = 25(1 - n)^{10}$
<b>Compaction index <math>C_c</math> (dimensionless)</b>	$\text{'sh'} : C_c = 0.7e + 0.44$ $\text{'shsd'} : C_c = 0.5e + 0.4$ $\text{'sd'} : C_c = 0.15e + 0.35$
<b>Mineralogy</b>	$\text{'sh'} : \text{Smectite\_Na } 30 \%$ $\text{'shsd'} : \text{Smectite\_Na } 15 \%$ $\text{'sd'} : \text{Smectite\_Na } 0 \%$

228

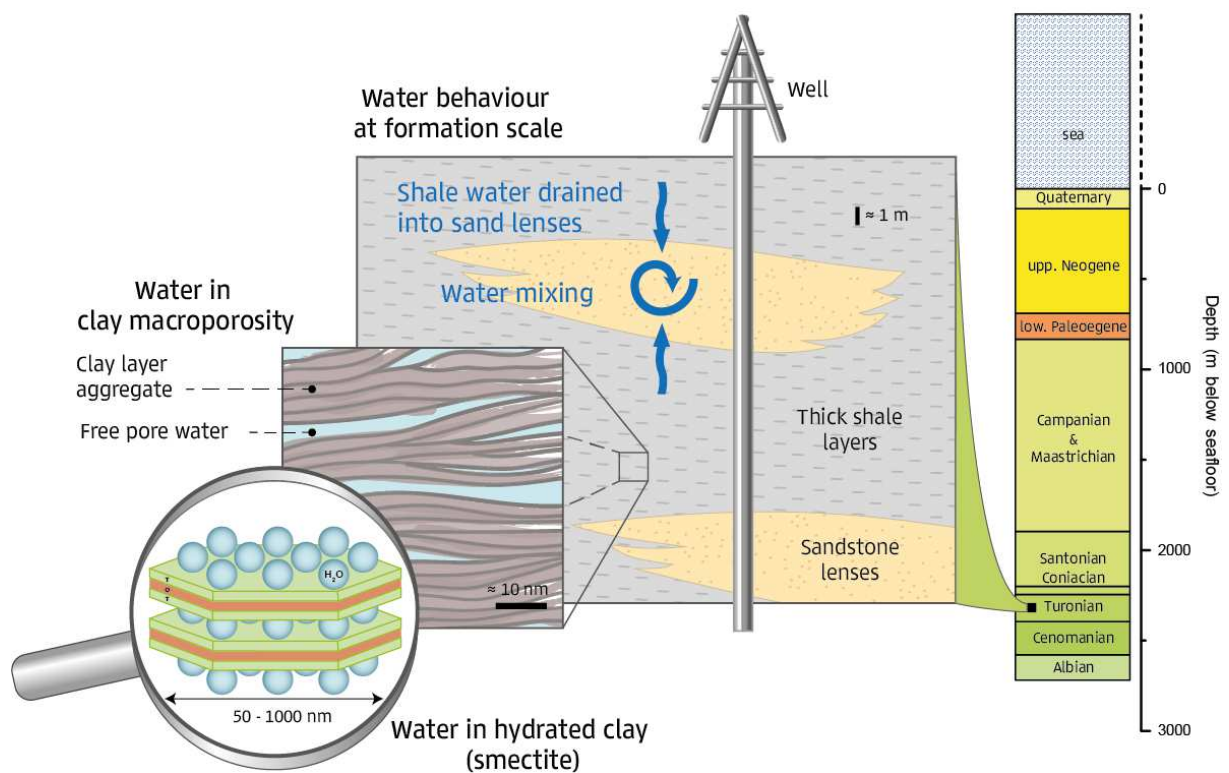
229

230 **Geological context** – Sand lenses draining water produced in shale  
 231 layers

232 Intercalations of sandstone lenses in thick shale layers of the Cenomanian, Turonian and Santonian  
 233 ages were found in the transform margin context of the Gulf of Guinea (Antobreh et al., 2009; Mascle  
 234 & Blarez, 1987). The exploration well is located offshore at a water depth of about 2000 m. The well  
 235 is drilled through a sediment thickness of about 2700 m. Several sandstone lenses 3 to 20 m thick  
 236 were intercalated between thicker shale layers 5 to 143 m thick in marine deposits corresponding to  
 237 transgressive sequences during the first connections with the Tethysian domain, during the opening  
 238 of the equatorial Atlantic Ocean. The sandstone corresponds to subarkose sandstones in the Folk

239 classification and present a porosity between 10 and 20 % for a permeability generally higher than 1  
 240 milliDarcy ( $10^{-15} \text{ m}^2$ ). Shale layers consist in claystones composed of 30 to 45 % of clay minerals and  
 241 mica, depending on the samples. Quartz and feldspars are the other main constituents. The smectite  
 242 is montmorillonite showing octahedral substitutions. Permeability between 0.0005 and 0.1 milliDarcy  
 243 were measured on the argillaceous sandstone facies but no measurements were made on samples  
 244 richer in clay minerals of the claystone facies.

245 Figure 1 schematically presents the geometry of the sandstone lenses intercalated in thicker shale  
 246 layers. The water released by the shales drains into the sandstone lenses where mixing with the  
 247 initial porewater can occur. It is therefore thought that information on the fluid evolution can be  
 248 deduced from water samples taken in the sandstone lenses at different depths.



249  
 250 *Figure 1: Schematic representation of the sediment geometry crossed by the well in the sediments of the Santonian,*  
 251 *Coniacian and Turonian ages with sandstone lenses intercalated between thicker shale layers. Fluids expelled from the shale*  
 252 *are drained and mixed in the sandstone lenses. Water in the clayrock is distributed between the water in the macroporosity,*  
 253 *expulsed by compaction, and the water in the interlayer space of smectite crystals, released during smectite dehydration.*

## 254 Well data suggesting clay dehydration

255 Several chemical and isotopic parameters measured on the water sampled in different sandstone  
 256 lenses after the borehole drilling suggest that clay dehydration occurred in the shale layers (Figure 2,  
 257 Table 5). A salinity decrease is observed with increasing depth, where the total dissolved salt (TDS)

258 content decreases from 18 to 5 g/L between about 2000 m and 2600 m deep, below the seafloor.  
259 Concomitantly to this salinity decrease, an increase in the  $\delta^{18}\text{O}\text{-H}_2\text{O}$  isotopic signature is observed.  
260 The shallower water sample (sample 1 in Figure 2) has a  $\delta^{18}\text{O}\text{-H}_2\text{O}$  signature of +0.6 ‰ vs SMOW  
261 (Standard Mean Ocean Water), close to reference 0 ‰  $\delta^{18}\text{O}\text{-H}_2\text{O}$  for seawater. The  $\delta^{18}\text{O}\text{-H}_2\text{O}$   
262 signature increases up to +7.1 ‰ vs SMOW in the deeper water samples. This increase of the  $\delta^{18}\text{O}\text{-H}_2\text{O}$   
263 signature can be explained by a release of positive  $\delta^{18}\text{O}$  during clay dehydration or alteration  
264 ( $\delta^{18}\text{O}$  of smectite ranges between +17 and +26 ‰ (Savin & Lee, 1988; Sheppard & Gilg, 1996)).  
265 Combined with the observed salinity decrease, the  $\delta^{18}\text{O}\text{-H}_2\text{O}$  signature evolution suggests a two-step  
266 evolution. First, the seawater trapped in the sediment is diluted without modifying its  $\delta^{18}\text{O}\text{-H}_2\text{O}$   
267 isotopic signature. This dilution can be attributed to the water produced by the surrounding shale  
268 layers during compaction and possibly affected by ultrafiltration process (Kharaka & Berry, 1973).  
269 Secondly, the salinity of sandstone lenses continues to decrease together with an increase of the  
270  $\delta^{18}\text{O}\text{-H}_2\text{O}$ . The smectite dehydration produces pure water with an elevated  $\delta^{18}\text{O}\text{-H}_2\text{O}$  signature  
271 causing the dilution and the rise of the  $\delta^{18}\text{O}\text{-H}_2\text{O}$  signature.

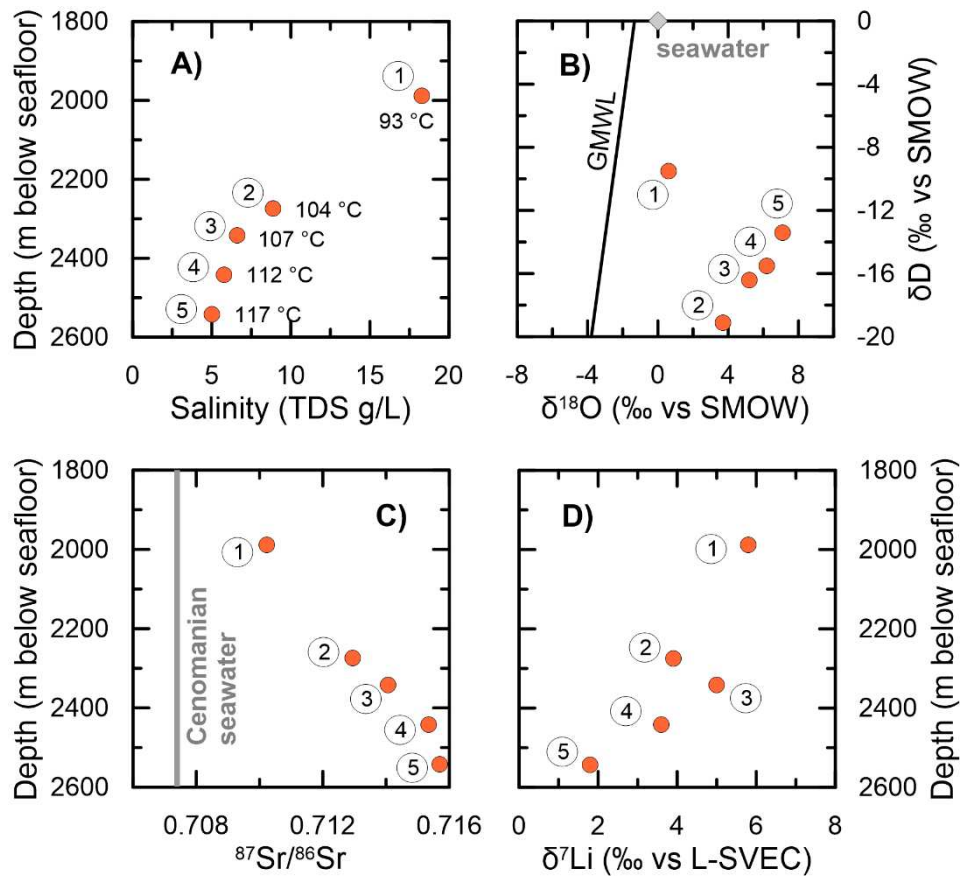
272 The  $\delta\text{D}\text{-H}_2\text{O}$  isotopic signature evolution (Figure 2) first shows a decrease from -9.5 ‰ to -19.1 ‰  
273 between the two shallower samples 1 and 2 and then an increase to -13.4 ‰ for the deeper sample.  
274 The causes of  $\delta\text{D}\text{-H}_2\text{O}$  evolution are more complex to identify because  $\delta\text{D}$  varies over a large range of  
275 isotopic signatures in smectite ( $\delta\text{D}$  from -95 ‰ to +33 ‰ in smectite (Capuano, 1992; Savin &  
276 Epstein, 1970)) and the induced variation can be overprinted by other factors, such as the interaction  
277 with alkane gases or the degradation of organic matter.

278 Insights on the water-rock interactions are given by the water chemistry evolution. In Figure 3, the  
279 water composition is reported as ratio of reactive species content (Na, Ca, Mg and K) in relation to a  
280 conservative species content (Cl) to distinguish the reactive processes from transport and dilution  
281 processes. The increase with depth of the Na/Cl, Ca/Cl, Mg/Cl and K/Cl content ratio indicates the  
282 dissolution of primary mineral phases containing Na, Ca, Mg and K, such as feldspars, micas or clay  
283 minerals, not followed by large precipitations of aluminosilicate phases. This identified trend in the  
284 diagenesis in the sedimentary pile is confirmed by petrographic observations in samples that show  
285 only little precipitations of kaolinite as diagenetic formation of aluminosilicate phases. The main  
286 authigenic minerals being observed are quartz and calcite. The fluid chemistry evolution does not  
287 reflect smectite-to-illite transformation, with an observed increase with depth of the K content in  
288 relation to the Cl content, while a decrease is expected if K is used for illite formation. In addition, the  
289 only 3 mineralogical analyses performed on shale layers of the sedimentary pile do not show a  
290 decrease in smectite content and an increase in illite content in the interstratified illite/smectite. It

291 therefore appears that illitisation does not take place to a large extent and can be neglected in our  
292 analysis.

293 No or little cross-formation flow in the sedimentary pile between the different sand lenses is  
294 suggested by the  $^{87}\text{Sr}/^{86}\text{Sr}$  isotopic ratio and the  $\delta^7\text{Li}$  isotopic signature measured on the sampled  
295 water (Figure 2). The  $^{87}\text{Sr}/^{86}\text{Sr}$  isotopic ratio increases with depth, at values higher than the  
296 theoretical  $^{87}\text{Sr}/^{86}\text{Sr}$  ratio of Cenomanian seawater. This increase of the  $^{87}\text{Sr}/^{86}\text{Sr}$  is likely to be due to  
297 the alteration of feldspar and clay minerals that release strontium richer in  $^{87}\text{Sr}$ , whose alteration  
298 increases with depth. The  $\delta^7\text{Li}$  isotopic signature in the water samples decreases with depth, from  
299 +5.8 ‰ in the shallower water sample (sample 1) to +1.8 ‰ in the deepest sample. These  $\delta^7\text{Li}$   
300 signatures are lower than the signature of modern seawater (+31 ‰ vs L-SVEC) and their range is  
301 compatible with an interaction with minerals of sedimentary rocks, such as clays. The decrease of the  
302  $\delta^7\text{Li}$  indicates the progress of the water/rock interaction with depth. The record of these progressive  
303 increase of  $^{87}\text{Sr}/^{86}\text{Sr}$  and decrease of  $\delta^7\text{Li}$  indicate the absence of connexion or a restricted connexion  
304 between the different sampled sand lenses. The hydrogeological media around each sand reservoir is  
305 thus closed, with little water flow and transport between the sand lenses and the surrounding shale  
306 layers (Figure 1).

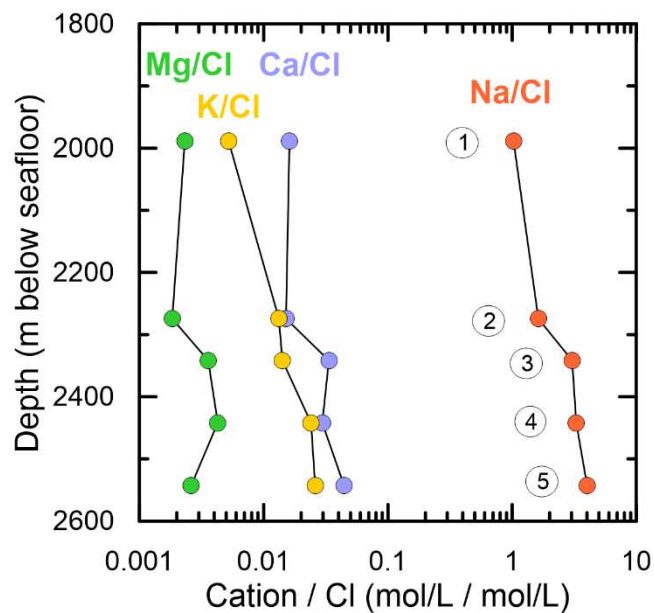
307



308

309 *Figure 2: Data for water samples from the well showing: a) decreasing salinity with depth; b)  $\delta D$  as a function of the  $\delta^{18}O$*   
 310 *water isotope signature at different depths. The reference seawater signature and the global meteoric water line (GMWL)*  
 311 *are also shown; c)  $^{87}Sr/^{86}Sr$  isotopic ratio increasing with depth and deviating from the ratio of the Cenomanian seawater;*  
 312 *and d)  $\delta^7Li$  isotopic signature decrease with depth. The circled numbers identify the five different water samples taken in the*  
 313 *well.*

314



315

316 *Figure 3. Water chemistry data from the five water samples taken in the well in sand lenses (identified by circled numbers).*  
 317 *The evolution of the concentration ratios (Na/Cl, Ca/Cl, Mg/Cl and K/Cl) helps identified the water/rock interactions within*  
 318 *the sedimentary pile.*

319 *Table 5: Data from water samples taken at different depth in the well: temperature, chemical composition and isotopic*  
 320 *signatures.*

	Temperature (°C)	Salinity TDS (g/L)	$\delta^{18}\text{O-H}_2\text{O}$ (‰ vs SMOW)	$\delta\text{D-H}_2\text{O}$ (‰ vs SMOW)	$^{87}\text{Sr}/^{86}\text{Sr}$	$\delta^7\text{Li}$ (‰ vs LSVEC)	$\text{Na}^+$ (mg/L)	$\text{K}^+$ (mg/L)	$\text{Ca}^{++}$ (mg/L)	$\text{Mg}^{++}$ (mg/L)	$\text{Cl}^-$ (mg/L)
Sample 1	93	18.27	+0.6	-9.5	0.7102	+5.8	5430	47	149	13	8177
Sample 2	104	8.89	+3.7	-19.1	0.7130	+3.9	2594	36	42	3.1	2461
Sample 3	107	6.61	+5.2	-16.4	0.7141	+5.0	1771	14	34	2.2	899
Sample 4	112	5.77	+6.2	-15.5	0.7153	+3.6	1522	19	24	2.1	717
Sample 5	117	5.02	+7.1	-13.4	0.7157	+1.8	1450	16	28	1.4	559

321

322

323 **Model results** – Reproducing the water isotope, salinity evolution and  
 324 overpressure considering smectite dehydration during sedimentary  
 325 pile burial

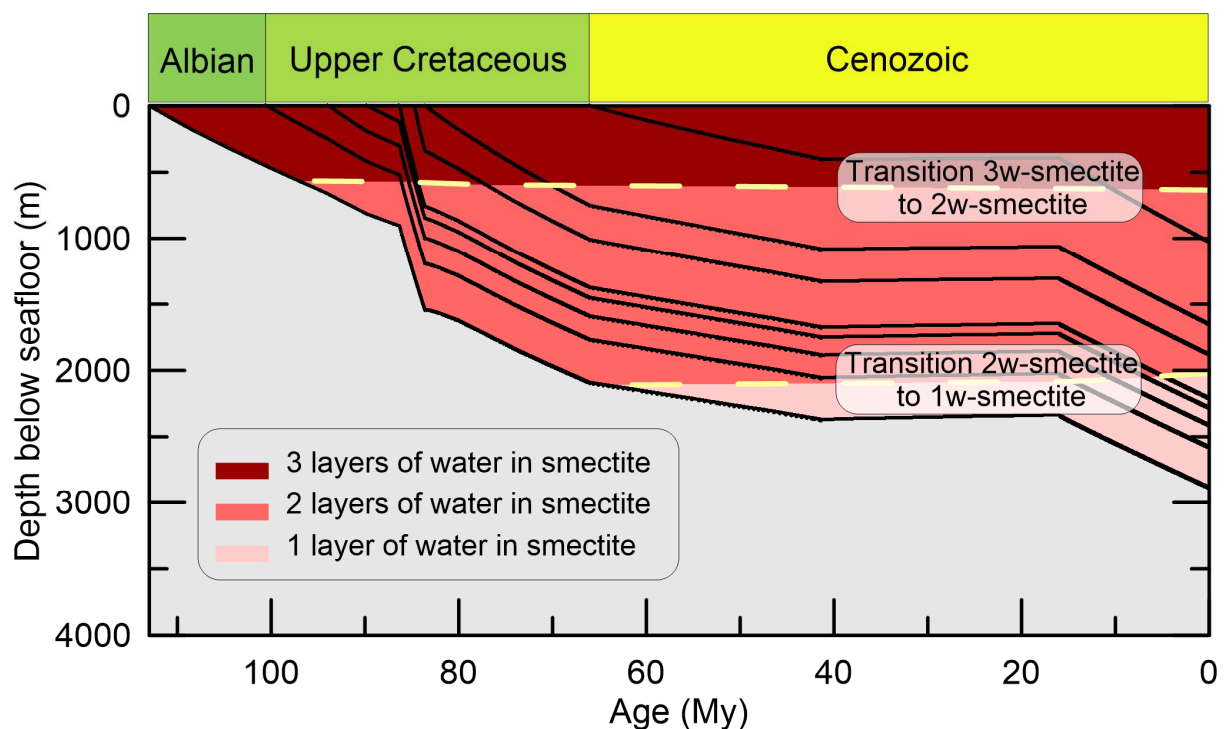
326 The water salinity and its isotopic composition in the sandstone lenses can be influenced by several  
 327 processes such as the expulsion of water during shale compaction, the release of water during  
 328 smectite dehydration and mixing of water from the sandstone and the shale. To individualise the  
 329 effect of smectite dehydration on the fluid evolution, it is necessary to consider these different  
 330 effects together and establish the water budget in the sedimentary pile. To this end, we calculated  
 331 the water production by smectite dehydration with a model reproducing the deposition of  
 332 sediments, the compaction of these sediments, the temperature increase with burial and the water  
 333 flow and pressure evolution in the sedimentary pile (Tremosa et al., 2020).

334 **Burial and smectite dehydration**

335 Our 1D forward modelling of sediment burial is performed based on the present-day lithological log  
 336 that identifies the thickness and lithology of the successive deposited lithological layers and on the  
 337 dating of stratigraphic surfaces that allows varying sedimentation rates to be calculated over time.  
 338 Sedimentation, compaction and pressure and temperature evolution in the sedimentary pile are then  
 339 reproduced since the Albian (Figure 5). Burial simulation coherence is assessed by comparison with  
 340 the present-day recorded thickness, porosity and temperatures profiles.



341 The calculated temperature and pressure evolutions over time allow the smectite dehydration model  
 342 to be applied (Tremosa et al., 2020; Vidal & Dubacq, 2009). This model describes smectite  
 343 dehydration as three possible binary solid solutions between hydrated and dehydrated smectite end-  
 344 members. The hydrated smectite can have 1, 2 or 3 layers of water in the smectite interlayer space,  
 345 depending on the calculated thermodynamic stability of each hydrated smectite for given  
 346 temperature and pressure conditions. With increasing temperature, smectite dehydrates according  
 347 to the most stable solid solution between hydrated and dehydrated smectite. However, at the  
 348 temperature transition between two stability domains of solid solutions, a consequent release of  
 349 water occurs because hydrated smectite loses one full layer of interlayer water. The thermodynamic  
 350 model is based on the standard state properties of hydrated and dehydrated smectite end-members  
 351 and integrates excess parameters for non-ideal solid solutions. Its results are in fair agreement with  
 352 the smectite dehydration experiments (Vidal & Dubacq, 2009). The release of water by smectite  
 353 dehydration is then simulated over the geological time across the investigated sedimentary pile  
 354 (Figure 4).

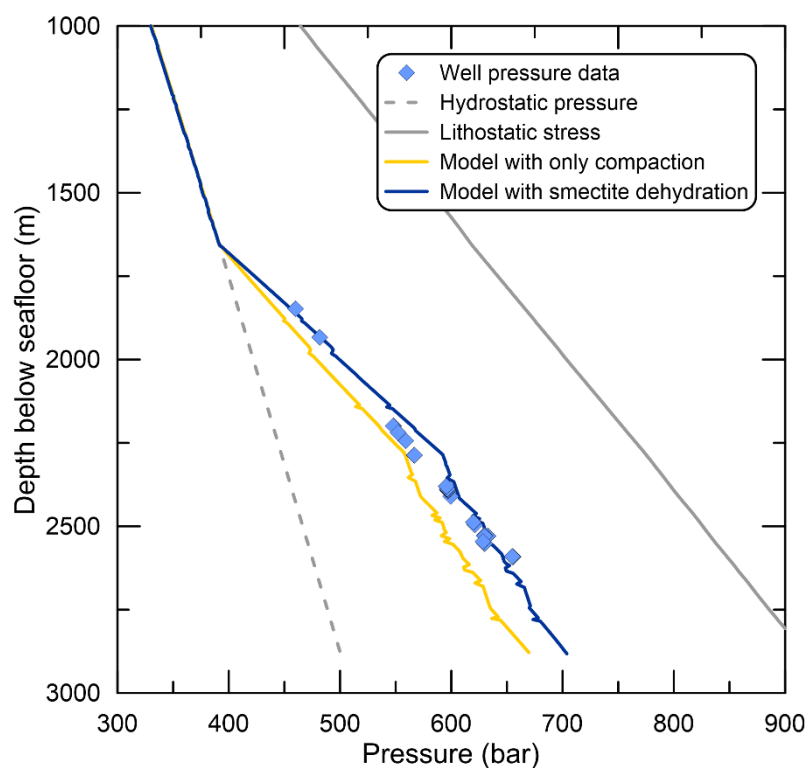


355  
 356 *Figure 4: Evolution of the stable hydrated solid solution end-member in the smectite dehydration model as a function of*  
 357 *sediment burial from the Albian to the present day. The black lines correspond to the depth evolution over time of the*  
 358 *different stratigraphic surfaces and the grey area to the basement of the sedimentary pile, taken from the modelled domain.*

### 359 Pressure profile

360 Pore pressure evolves in the sedimentary pile because of sediment compaction which induces a  
 361 porosity reduction and a compression of the water filling the pores, water expansion during

362 temperature increase, water release by smectite dehydration and advective water flow. An  
 363 overpressure of 150 to 170 bar is observed in the Turonian reservoirs at a depth of around 2500 m  
 364 below the seafloor. The model that considers smectite dehydration in addition to compaction and  
 365 temperature increase reproduces the present-day pressure profile (Figure 5). When smectite  
 366 dehydration is omitted in the model, the pressure is about 40 bar lower, indicating that smectite  
 367 dehydration contributes to about 25 % of the recorded overpressure. The model indicates that the  
 368 overpressure is generated during the last burial episode that started 16 My ago. The transition of  
 369 smectite hydrated with two layers of water to one layer of water is crossed in the Cenomanian to  
 370 Santonian layers during this burial event (Figure 4), leading to a consequent release of water that  
 371 contributes to the pore pressure.



372  
 373 *Figure 5: Measured and calculated pressure profiles at present day, with and without smectite dehydration in addition to*  
 374 *compaction. Hydrostatic and overburden pressures are shown for comparison.*

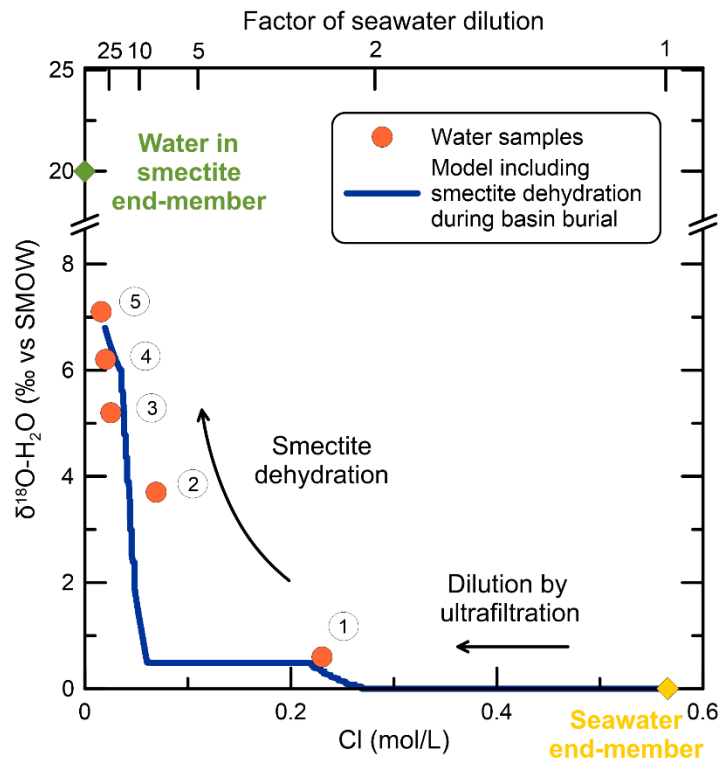
### 375 Chemical and isotopic evolution of fluids

376 The evolution of the chemical and isotopic composition of water in the sandstone lenses is calculated  
 377 by mixing, in the sandstone levels, the water originated from the surrounding shale layers, in order to  
 378 respect the water balance within the geometry and the evolution of the considered sedimentary pile.  
 379 Dilution of the initial seawater in the sandstone lenses by compaction water flowing from the shale  
 380 layers or produced by smectite dehydration is simulated when intrinsic permeability of overlying  
 381 shale drops below  $10^{-20}$  m<sup>2</sup>, by effect of compaction. This criterion on the permeability of the shale

382 assumes that the hydrogeological media formed of a sandstone lens and its surrounding shale layers  
383 becomes closed to external flow below this permeability. It corresponds to a burial depth of about  
384 1900 m and to the depth of the overpressure roof in the present-day pressure profile.

385 The water isotopic signature remains unchanged during the dilution by compaction water because  
386 the water trapped in the porosity of both shale and sandstone sediments was seawater with a  $\delta^{18}\text{O}$ -  
387  $\text{H}_2\text{O}$  signature of 0 ‰. Besides, smectite dehydration releases water with a positive  $\delta^{18}\text{O}$ - $\text{H}_2\text{O}$   
388 signature of +20 ‰ SMOW, in agreement with the  $\delta^{18}\text{O}$  signature of smectite referenced in the  
389 literature (Savin & Lee, 1988; Sheppard & Gilg, 1996).

390 The model considering smectite dehydration during basin burial reproduces, in good agreement, the  
391 related evolution with a depth of  $\delta^{18}\text{O}$ - $\text{H}_2\text{O}$  signature and salinity of sampled water from sandstone  
392 levels in the well (Figure 6). During the modelling of the burial, the salinity in the sandstone layer  
393 corresponding to the deepest sampled sandstone lens first decreases due to seawater dilution  
394 without changing its isotopic signature and then decreases together with an increase in the  $\delta^{18}\text{O}$   
395 signature of water. The model captures the effect of releasing water with positive  $\delta^{18}\text{O}$  during  
396 smectite dehydration. The mixing of this released water in the associated sandstone level follows the  
397 measured  $\delta^{18}\text{O}$ - $\text{H}_2\text{O}$  signature to obtain a  $\delta^{18}\text{O}$ - $\text{H}_2\text{O}$  of +6.8 ‰ for the deepest sampled sandstone  
398 lens. The transition of a hydrated smectite with 2 layers of water to 1 layer of water is modelled at a  
399 depth between the first and the second sampled sandstone lenses, with the associated freshening  
400 calculated. It is worth noting that the  $\delta^{18}\text{O}$ - $\text{H}_2\text{O}$  signature and salinity evolution are obtained for the  
401 corresponding shale and sandstone thickness, smectite content in shale and timing of smectite  
402 dehydration.



403

404 *Figure 6:  $\delta^{18}\text{O-H}_2\text{O}$  isotopic signature compared to the salinity (concentration of chlorine) of the sampled water in sandstone*  
 405 *lenses of the well. The model accounting for smectite dehydration during basin burial reproduces the evolution of water*  
 406 *samples observed with depth. The salinity decrease is also shown as a factor of seawater dilution. Circled numbers*  
 407 *correspond to the water samples, as in Figure 2.*

## 408 Discussion

409 First evidence of smectite dehydration at the scale of the sedimentary pile

410 The present results constitute the first consistent evidence of the influence of smectite dehydration  
 411 on the fluid salinity and pressure in a sedimentary basin. The model coherence in reproducing the  
 412  $\delta^{18}\text{O-H}_2\text{O}$  isotopic signature, the salinity and the pressure profile supports this influence of smectite  
 413 dehydration. Up to now, the influence of smectite dehydration was advanced for the evolution of the  
 414 chemical composition and isotopic signature of the sediments porewater (Hanor, 1994) or for its  
 415 contribution to the fluid overpressure (Tremosa et al., 2020), but both effects were not simulated  
 416 together. The burial of Cretaceous sediments was modelled in the Gulf of Guinea and the fluid  
 417 pressure and smectite dehydration were simulated during this burial. Calculations showed that  
 418 smectite dehydration explains about a quarter of the present-day recorded overpressure, in addition  
 419 to disequilibrium compaction and temperature increase. Water freshening caused by ultrafiltration  
 420 flow and by smectite dehydration can reproduce the salinity evolution with depth in sandstone  
 421 lenses surrounded by thick shale layers. The salinity decrease is accompanied by an increase in the  
 422  $\delta^{18}\text{O-H}_2\text{O}$  signature that exactly matches the  $\delta^{18}\text{O-H}_2\text{O}$  signature evolution modelled by the release of

423 water by smectite dehydration during the burial of the sedimentary pile, where the water budget  
424 during smectite dehydration and its timing are respected.

425 Uncertainties on the isotopic signature of smectite interlayer water

426 A calculation hypothesis was made on the  $\delta^{18}\text{O}$  signature of the water released during smectite  
427 dehydration. Relatively few data are available on the  $\delta^{18}\text{O}$  signature of smectite and these signatures  
428 can present some contamination because of the difficulties in purifying smectite and clay minerals  
429 (Sheppard & Gilg, 1996). However,  $\delta^{18}\text{O}$  signatures for smectite ranging between +17 and +26 ‰  
430 (Savin & Lee, 1988) seem reasonable. It is more difficult to estimate the  $\delta^{18}\text{O}$  signature of smectite  
431 interlayer water because the interlayer water can be lost during sample preparation or interstitial  
432 water can remain sorbed on the clay mineral (Sheppard & Gilg, 1996). In the literature, it has been  
433 claimed that the exchange between porewater and interlayer water is fast and that the  $\delta\text{D}$  and  $\delta^{18}\text{O}$   
434 signatures of interlayer water do not provide geological information (Savin & Epstein, 1970).  
435 However, this affirmation is in disagreement with studies on the interstitial water of mud volcanoes  
436 that showed a clear influence of smectite dehydration on their water isotope signature (Dählmann &  
437 Lange, 2003; Hensen et al., 2007) and rather suggest that the  $\delta^{18}\text{O}$  signature of interlayer water is  
438 close to the  $\delta^{18}\text{O}$  signature of structural smectite. The distinction between structural and interlayer  
439  $\delta^{18}\text{O}$  isotopic signatures hence remains to be investigated, by dedicated experiments in order to  
440 distinguish between the production of pore and interlayer water in a smectite (Fernández et al.,  
441 2014) or from insights given by molecular dynamics simulations.

442 Discarding other sources of water isotopic signature variations

443 The influence on the  $\delta^{18}\text{O}\text{-H}_2\text{O}$  isotopic signature evolution of other water-rock interaction  
444 (carbonate precipitation and smectite illitisation) or transport (ultrafiltration) processes can be  
445 discarded in the sedimentary system under consideration. The isotopic fractionation during the  
446 precipitation of carbonate minerals is known to modify the  $\delta^{18}\text{O}\text{-H}_2\text{O}$  isotopic signature. In the  
447 studied lithological column, petrographic observations indicate an early cementation of calcite,  
448 during the early stage of burial and compaction, at temperature estimated at about 30°C. If the  $\delta^{18}\text{O}\text{-}$   
449  $\text{H}_2\text{O}$  isotopic signature has been modified at that time because of calcite precipitation, it occurred in  
450 a hydraulic open system, where water can be flushed. The simulation scenario considers the dilution  
451 and isotopic shift when the system becomes closed on a hydraulic point of view, namely, when the  
452 intrinsic permeability of the overlying shale layer becomes lower than  $10^{-20} \text{ m}^2$ , corresponding to a  
453 burial depth of about 1900 m. Hence, the precipitation of early carbonates is not expected to change  
454 the calculated  $\delta^{18}\text{O}\text{-H}_2\text{O}$  evolution since this precipitation occurred before. The isotopic fractionation  
455 during the smectite-to-illite transformation can also lead to an increase of the  $\delta^{18}\text{O}\text{-H}_2\text{O}$  isotopic

456 signature at increasing temperature (Suchecki & Land, 1983). The data on mineralogy and water  
457 chemistry available from the well indicate an absence of noticeable illitisation. Consequently, the  
458 recorded  $\delta^{18}\text{O}\text{-H}_2\text{O}$  isotopic signature in the sand lenses is certainly not impacted by smectite  
459 illitisation process. During ultrafiltration flow, a flow of water with solute transport partially impeded  
460 because of the membrane behaviour of the shale, a moderate isotopic fractionation can occur  
461 (Agrinier et al., 2021; Coplen & Hanshaw, 1973). However, the effect of this isotopic fractionation  
462 during ultrafiltration is not clearly established, with contradictory studies reporting a depletion or an  
463 enrichment of the  $\delta^{18}\text{O}\text{-H}_2\text{O}$  signature of the water flowing out of the shale (Agrinier et al., 2021). The  
464 effect of ultrafiltration on  $\delta^{18}\text{O}\text{-H}_2\text{O}$  isotopic signature is difficultly distinguished from the effect of  
465 water-rock interactions. In the simulations executed in the present study, a flow of fresh water  
466 expelled from the shale layers that can correspond to ultrafiltration is mimicked by considering a  
467 progressive dilution of the water in the sand lenses. Since the effect of ultrafiltration on the  $\delta^{18}\text{O}\text{-H}_2\text{O}$   
468 isotopic signature remains unclear and probably weak and because the simulation of ultrafiltration  
469 process is complex, this possible effect has not been considered in this analysis.

#### 470 Likely occurrence of smectite dehydration compared to illitisation

471 In studies on fluid evolution or overpressure generation by the water released by smectite, the  
472 analysis is often restricted to smectite-to-illite transformation, but more rarely consider the  
473 dehydration of interlayer smectite, notwithstanding that interlayer dehydration is  
474 thermodynamically and kinetically easier than illitisation. However, even in high pressure  
475 environments in which the total dehydration is predicted at a temperature of 300°C or higher, the  
476 main dehydration steps (3 layers of water to 2 and 2 layers of water to 1) take place at temperatures  
477 lower than 150°C (Vidal & Dubacq, 2009), concomitantly to smectite illitisation. The formation of  
478 illite consumes potassium and, then, a depletion of potassium in the porewater indicates the  
479 occurrence of a significant illitisation. In the present study, such a marker of illitisation was not  
480 observed from the K/Na ratio and smectite-to-illite transformation was ruled out. At the contrary,  
481 when the porewater composition shows a consumption of potassium (Vanneste et al., 2011),  
482 smectite illitisation is rationally to consider in the fluid budget analysis.

#### 483 Implications on fluid budget in sedimentary basins

484 Our demonstration of the identification of smectite dehydration as the source of fluid modification in  
485 the studied sedimentary pile in the Gulf of Guinea highlights the importance of considering coupled  
486 approaches to understand the origin of fluids in sedimentary basins. Assessing the fluid budget in a  
487 sedimentary basin requires dedicated and integrated studies accounting for the temporal and spatial  
488 production of fluid and using a sound and calibrated model of fluid production. Notably, the water

489 release during smectite dehydration was calculated using a predictive thermodynamic model  
490 calibrated on experimental data. Thanks to this approach, it is possible to use the water's isotopic  
491 evolution as a hydrogeological constraint in regional studies of fluid migration.

492

## 493 Conclusions

494 Smectite dehydration was advanced as a process that can influence the fluid pressure and the water  
495 composition and isotopic signature in sedimentary basins, but a direct evidence has been lacking up  
496 to now. In the sedimentary pile studied in the Gulf of Guinea, the dehydration of smectite interlayer  
497 water influences the overpressure and the porewater composition and isotopic signature. This  
498 influence was evidenced thanks to the simulation of the water production during the burial using a  
499 modelling approach that couples hydraulic, mechanical, thermal, thermodynamic and isotopic  
500 processes. In the model, smectite dehydration is described using a thermodynamic model and driven  
501 by the temperature and pressure changes during the burial where the volume of water released  
502 depends on the geometry of the sedimentary pile. This spatial and temporal fluid budget shows that  
503 smectite dehydration contributes to about 25 % of the present-day overpressure of 150 to 170 bar,  
504 together with classical purely hydro-mechanical processes. In addition to influence the overpressure,  
505 smectite dehydration induces a dilution of porewater salinity and an increase of the  $\delta^{18}\text{O}\text{-H}_2\text{O}$   
506 isotopic signature with increasing depth. Unique data from a deep well of more than 5000 m of total  
507 depth, including 2000 m of water, were used in our analysis. The simulation of these hydraulic,  
508 chemical and isotopic markers are goods clues of the on-going geological process in the sedimentary  
509 basin.

510 The influence of smectite dehydration is specific to each sedimentary system and evaluating the  
511 contribution of smectite dehydration requires performing a water budget involving smectite  
512 dehydration during the burial of the studied sedimentary pile. Our study is focused on the evaluation  
513 of fluid migration in sedimentary basins for the potential exploitation of energy fluids but it is also of  
514 interest to have a better understanding of the effect of smectite dehydration in other contexts. For  
515 example, our findings and the methodology undertaken here can be directly be applied in studies on  
516 the behaviour of fluids in subduction zones or in mud volcanoes.

517

## 518 Acknowledgments

519 This work was funded by TOTAL S.A. and BRGM. Céline Roux is thanked for the figure artwork and  
520 Sally Ferguson for the English language editing. Editor M. Kersten and one anonymous reviewer are  
521 acknowledged for their constructive comments on the manuscript.

## 522 Author contributions

523 J.T. adapted a previous version of the SURP code, made the coupled modelling and interpreted the  
524 results. H.G. calculated the thermodynamic parameters describing smectite dehydration. E.C.G. took  
525 the water samples, ordered the isotopic and chemical analysis and emitted the hypothesis that the  
526 isotopic and salinity data reflected smectite dehydration. J.T. wrote the early version of the  
527 manuscript. E.C.G. and H.G. contributed to the writing of the manuscript. All authors participated to  
528 conceptualize this study and commented on the final version of the manuscript

## 529 References

- 530 Agrinier, P., Bonifacie, M., Bardoux, G., Lucazeau, F., Giunta, T., & Ader, M. (2021). Chlorine isotope  
531 data of chlorides challenge the pore fluid paradigm. *Geochimica Cosmochimica Acta*, *300*,  
532 258–278. <https://doi.org/10.1016/j.gca.2021.02.034>
- 533 Antobreh, A. A., Faleide, J. I., Tsikalas, F., & Planke, S. (2009). Rift–shear architecture and tectonic  
534 development of the Ghana margin deduced from multichannel seismic reflection and  
535 potential field data. *Marine and Petroleum Geology*, *26*(3), 345–368.  
536 <https://doi.org/10.1016/j.marpetgeo.2008.04.005>
- 537 Audet, D. M. (1995). Mathematical modelling of gravitational compaction and clay dehydration in  
538 thick sediment layers. *Geophysical Journal International*, *122*(1), 283–298.  
539 <https://doi.org/10.1111/j.1365-246X.1995.tb03554.x>
- 540 Bekins, B. A., McCaffrey, A. M., & Dreiss, S. J. (1995). Episodic and constant flow models for the origin  
541 of low-chloride waters in a modern accretionary complex. *Water Resources Research*, *31*(12),  
542 3205–3215. <https://doi.org/10.1029/95WR02569>



543 Bjørlykke, K., Jahren, J., Aagaard, P., & Fisher, Q. (2010). Role of effective permeability distribution in  
544 estimating overpressure using basin modelling. *Marine and Petroleum Geology*, 27(8), 1684–  
545 1691. <https://doi.org/10.1016/j.marpetgeo.2010.05.003>

546 Blanc, P., Vieillard, P., Gailhanou, H., Gaboreau, S., Gaucher, E., Fialips, & Giffaut, E. (2015). A  
547 generalized model for predicting the thermodynamic properties of clay minerals. *American*  
548 *Journal of Science*, 315, 734–780.

549 Boschetti, T., Angulo, B., Cabrera, F., Vásquez, J., & Montero, R. L. (2016). Hydrogeochemical  
550 characterization of oilfield waters from southeast Maracaibo Basin (Venezuela): Diagenetic  
551 effects on chemical and isotopic composition. *Marine and Petroleum Geology*, 73, 228–248.  
552 <https://doi.org/10.1016/j.marpetgeo.2016.02.020>

553 Brown, K. M., Saffer, D. M., & Bekins, B. A. (2001). Smectite diagenesis, pore-water freshening, and  
554 fluid flow at the toe of the Nankai wedge. *Earth and Planetary Science Letters*, 194(1), 97–  
555 109. [https://doi.org/10.1016/S0012-821X\(01\)00546-5](https://doi.org/10.1016/S0012-821X(01)00546-5)

556 Bruce, C. H. (1984). Smectite dehydration; its relation to structural development and hydrocarbon  
557 accumulation in northern Gulf of Mexico basin. *AAPG Bulletin*, 68, 673–683.

558 Capuano, R. . (1992). The temperature dependence of hydrogen isotope fractionation between clay  
559 minerals and water: Evidence from a geopressured system. *Geochimica et Cosmochimica*  
560 *Acta*, 56(6), 2547–2554. [https://doi.org/10.1016/0016-7037\(92\)90208-Z](https://doi.org/10.1016/0016-7037(92)90208-Z)

561 Clayton, R. N., Friedman, I., Graf, D. L., Mayeda, T. K., Meents, W. F., & Shimp, N. F. (1966). The origin  
562 of saline formation waters: 1. Isotopic composition. *Journal of Geophysical Research*, 71(16),  
563 3869–3882. <https://doi.org/10.1029/JZ071i016p03869>

564 Colten-Bradley, V. A. (1987). Role of pressure in smectite dehydration; effects on geopressure and  
565 smectite-to-illite transformation. *AAPG Bulletin*, 71, 1414–1427.

566 Coplen, T. B., & Hanshaw, B. B. (1973). Ultrafiltration by a compacted clay membrane—I. Oxygen and  
567 hydrogen isotopic fractionation. *Geochimica Cosmochimica Acta*, 37(10), 2295–2310.  
568 [https://doi.org/10.1016/0016-7037\(73\)90105-1](https://doi.org/10.1016/0016-7037(73)90105-1)

569 Dählmann, A., & Lange, G. . de. (2003). Fluid–sediment interactions at Eastern Mediterranean mud  
570 volcanoes: a stable isotope study from ODP Leg 160. *Earth and Planetary Science Letters*,  
571 *212*(3), 377–391. [https://doi.org/10.1016/S0012-821X\(03\)00227-9](https://doi.org/10.1016/S0012-821X(03)00227-9)

572 Fernández, A. M., Sánchez-Ledesma, D. M., Tournassat, C., Melón, A., Gaucher, E. C., Astudillo, J., &  
573 Vinsot, A. (2014). Applying the squeezing technique to highly consolidated clayrocks for pore  
574 water characterisation: Lessons learned from experiments at the Mont Terri Rock Laboratory.  
575 *Applied Geochemistry*, *49*, 2–21. <https://doi.org/10.1016/j.apgeochem.2014.07.003>

576 Fitts, T. G., & Brown, K. M. (1999). Stress-induced smectite dehydration: ramifications for patterns of  
577 freshening and fluid expulsion in the N. Barbados accretionary wedge. *Earth and Planetary  
578 Science Letters*, *172*(1), 179–197. [https://doi.org/10.1016/S0012-821X\(99\)00168-5](https://doi.org/10.1016/S0012-821X(99)00168-5)

579 Franks, S. G., & Uchytíl, S. J. (2016). Geochemistry of formation waters from the subsalt Tubular Bells  
580 Field, offshore Gulf of Mexico: Implications for fluid movement and reservoir continuity.  
581 *AAPG Bulletin*, *100*(6), 943–967. <https://doi.org/10.1306/02101615027>

582 Hanor, J. S. (1994). Physical and chemical controls on the composition of waters in sedimentary  
583 basins. *Marine and Petroleum Geology*, *11*(1), 31–45. [https://doi.org/10.1016/0264-  
584 8172\(94\)90007-8](https://doi.org/10.1016/0264-8172(94)90007-8)

585 Henry, P., & Bourlange, S. (2004). Smectite and fluid budget at Nankai ODP sites derived from cation  
586 exchange capacity. *Earth and Planetary Science Letters*, *219*(1), 129–145.  
587 [https://doi.org/10.1016/S0012-821X\(03\)00694-0](https://doi.org/10.1016/S0012-821X(03)00694-0)

588 Hensen, C., Nuzzo, M., Hornibrook, E., Pinheiro, L. M., Bock, B., Magalhães, V. H., & Brückmann, W.  
589 (2007). Sources of mud volcano fluids in the Gulf of Cadiz—indications for hydrothermal  
590 imprint. *Geochimica et Cosmochimica Acta*, *71*(5), 1232–1248.  
591 <https://doi.org/10.1016/j.gca.2006.11.022>

592 Hüpers, A., & Kopf, A. J. (2012). Effect of smectite dehydration on pore water geochemistry in the  
593 shallow subduction zone: An experimental approach. *Geochemistry, Geophysics, Geosystems*,  
594 *13*(10). <https://doi.org/10.1029/2012GC004212>

595 Hüpers, A., Grathoff, G., Warr, L. N., Wemmer, K., Spinelli, G., & Underwood, M. B. (2019).  
596 Spatiotemporal Characterization of Smectite-to-Illite Diagenesis in the Nankai Trough  
597 Accretionary Prism Revealed by Samples From 3 km Below Seafloor. *Geochemistry,*  
598 *Geophysics, Geosystems, 20*(2), 933–951. <https://doi.org/10.1029/2018GC008015>

599 Kastner, M. J., Elderfield, H., Jenkins, W. J., Gieskes, J. M., & Gamo, T. (1993). Geochemical and  
600 isotopic evidence for fluid flow in the western Nankai subduction zone, Japan. In *Proceedings*  
601 *of the Ocean Drilling Program, Scientific Results, Vol. 131.*

602 Kharaka, Y. K., & Berry, F. A. P. (1973). Simultaneous flow of water and solutes through geological  
603 membranes—I. Experimental investigation. *Geochimica et Cosmochimica Acta, 37*(12), 2577–  
604 2603. [https://doi.org/10.1016/0016-7037\(73\)90267-6](https://doi.org/10.1016/0016-7037(73)90267-6)

605 Macpherson, G. L. (1992). Regional Variations in Formation Water Chemistry: Major and Minor  
606 Elements, Frio Formation Fluids, Texas. *AAPG Bulletin, 76*(5), 740–757.  
607 <https://doi.org/10.1306/BDF88C6-1718-11D7-8645000102C1865D>

608 Mascle, J., & Blarez, E. (1987). Evidence for transform margin evolution from the Ivory Coast-Ghana  
609 continental margin. *Nature, 326*(6111), 378–381. Retrieved from  
610 <https://doi.org/10.1038/326378a0>

611 Meunier, A., & Velde, B. (1989). Solid solution in I/S mixed-layer minerals and illite. *American*  
612 *Mineralogist, 74*, 1106–1112.

613 Morton, R. A., & Land, L. S. (1987). Regional Variations in Formation Water Chemistry, Frio Formation  
614 (Oligocene), Texas Gulf Coast1. *AAPG Bulletin, 71*(2), 191–206.  
615 <https://doi.org/10.1306/94886D6C-1704-11D7-8645000102C1865D>

616 Neuzil, C. E. (1995). Abnormal pressures as hydrodynamic phenomena. *American Journal of Science,*  
617 *295*, 742–786.

618 Nicot, J.-P., Gherabati, A., Darvari, R., & Mickler, P. (2018). Salinity Reversal and Water Freshening in  
619 the Eagle Ford Shale, Texas, USA. *ACS Earth and Space Chemistry, 2*(11), 1087–1094.  
620 <https://doi.org/10.1021/acsearthspacechem.8b00095>

621 Saffer, D. M., & McKiernan, A. W. (2009). Evaluation of in situ smectite dehydration as a pore water  
622 freshening mechanism in the Nankai Trough, offshore southwest Japan. *Geochemistry,*  
623 *Geophysics, Geosystems, 10*(2). <https://doi.org/10.1029/2008GC002226>

624 Savin, S. M., & Epstein, S. (1970). The oxygen and hydrogen isotope geochemistry of clay minerals.  
625 *Geochimica et Cosmochimica Acta, 34*(1), 25–42. [https://doi.org/10.1016/0016-](https://doi.org/10.1016/0016-7037(70)90149-3)  
626 [7037\(70\)90149-3](https://doi.org/10.1016/0016-7037(70)90149-3)

627 Savin, S. M., & Lee, M. (1988). Hydrous phyllosilicates. In S. W. Bailey (Ed.) (Vol. 19, pp. 189–223).  
628 Mineralogical Society of America.

629 Sclater, J. G., & Christie, P. A. F. (1980). Continental stretching: An explanation of the Post-Mid-  
630 Cretaceous subsidence of the central North Sea Basin. *Journal of Geophysical Research: Solid*  
631 *Earth, 85*(B7), 3711–3739. <https://doi.org/10.1029/JB085iB07p03711>

632 Sheppard, S. M. F., & Gilg, H. A. (1996). Stable isotope geochemistry of clay minerals: “The story of  
633 sloppy, sticky, lumpy and tough” Cairns-Smith (1971). *Clay Minerals, 31*(1), 1–24.  
634 <https://doi.org/10.1180/claymin.1996.031.1.01>

635 Suhecki, R. K., & Land, L. S. (1983). Isotopic geochemistry of burial-metamorphosed volcanogenic  
636 sediments, Great Valley sequence, northern California. *Geochimica Cosmochimica Acta,*  
637 *47*(8), 1487–1499. [https://doi.org/10.1016/0016-7037\(83\)90308-3](https://doi.org/10.1016/0016-7037(83)90308-3)

638 Tanikawa, W., Shimamoto, T., Wey, S., Lin, C., & Lai, W. (2008). Stratigraphic variation of transport  
639 properties and overpressure development in the Western Foothills, Taiwan. *Journal of*  
640 *Geophysical Research: Solid Earth, 113*(B12). <https://doi.org/10.1029/2008JB005647>

641 Tremosa, J., Gailhanou, H., Chiaberge, C., Castilla, R., Gaucher, E. C., Lassin, A., ... Claret, F. (2020).  
642 Effects of smectite dehydration and illitisation on overpressures in sedimentary basins: A  
643 coupled chemical and thermo-hydro-mechanical modelling approach. *Marine and Petroleum*  
644 *Geology, 111*, 166–178. <https://doi.org/10.1016/j.marpetgeo.2019.08.021>

645 Vanneste, H., Kelly-Gerreyn, B. A., Connelly, D. P., James, R. H., Haeckel, M., Fisher, R. E., ... Mills, R.  
646 A. (2011). Spatial variation in fluid flow and geochemical fluxes across the sediment–

647 seawater interface at the Carlos Ribeiro mud volcano (Gulf of Cadiz). *Geochimica et*  
648 *Cosmochimica Acta*, 75(4), 1124–1144. <https://doi.org/10.1016/j.gca.2010.11.017>

649 Vidal, O., & Dubacq, B. (2009). Thermodynamic modelling of clay dehydration, stability and  
650 compositional evolution with temperature, pressure and H<sub>2</sub>O activity. *Geochimica et*  
651 *Cosmochimica Acta*, 73(21), 6544–6564. <https://doi.org/10.1016/j.gca.2009.07.035>

652 Wilkinson, M., Crowley, S. F., & Marshall, J. D. (1992). Model for the evolution of oxygen isotope  
653 ratios in the pore fluids of mudrocks during burial. *Marine and Petroleum Geology*, 9(1), 98–  
654 105. [https://doi.org/10.1016/0264-8172\(92\)90007-2](https://doi.org/10.1016/0264-8172(92)90007-2)

655

656